

## Flow and Fracture in Drying Nanoparticle Suspensions

E. R. Dufresne,<sup>1,2</sup> E. I. Corwin,<sup>1,\*</sup> N. A. Greenblatt,<sup>1</sup> J. Ashmore,<sup>2</sup> D. Y. Wang,<sup>1,2</sup> A. D. Dinsmore,<sup>1,2,†</sup> J. X. Cheng,<sup>3</sup>  
X. S. Xie,<sup>3</sup> J. W. Hutchinson,<sup>2</sup> and D. A. Weitz<sup>1,2</sup>

<sup>1</sup>Department of Physics, Harvard University, Cambridge, Massachusetts 02138, USA

<sup>2</sup>DEAS, Harvard University, Cambridge, Massachusetts 02138, USA

<sup>3</sup>Department of Chemistry, Harvard University, Cambridge, Massachusetts 02138, USA

(Received 5 May 2003; published 24 November 2003)

Drying aqueous suspensions of monodisperse silica nanoparticles can fracture in remarkable patterns. As the material solidifies, evenly spaced cracks invade from the drying surface, with individual cracks undergoing intermittent motion. We show that the growth of cracks is limited by the advancement of the compaction front, which is governed by a balance of evaporation and flow of fluid at the drying surface. Surprisingly, the macroscopic dynamics of drying show signatures of molecular-scale fluid effects.

DOI: 10.1103/PhysRevLett.91.224501

PACS numbers: 47.55.Mh, 62.20.Mk, 68.08.Bc, 82.70.Dd

Drying suspensions are familiar, ubiquitous, and deceptively simple. As the solvent evaporates, they undergo a fluid to solid transition, leaving a film that is familiar to anyone who has spread a coat of paint or spilled a drop of coffee. However, when examined closely, this simple process displays rich phenomenology presenting a plethora of intriguing and important questions. Perhaps most importantly, enormous stress can develop during drying that can fracture the film; this has serious technological consequences as it can destroy the efficacy of coatings and limit the potential size of photonic crystals [1]. However, these cracks can also exhibit intriguing morphologies, including two-dimensional networks [2] and logarithmic spirals [3]. Crack formation has been widely studied in controlled experiments, and numerous models have been proposed to describe the qualitative features of crack morphology and the drying process responsible for cracking [2–7]. In contrast to the well understood drying mechanisms of gels [8], there is little consensus on even the most basic mechanisms of drying in suspensions. Furthermore, there is sparse quantitative comparison of theory and experiment to discern critically between the contradictory assumptions of various models. Without a quantitative understanding of the mechanisms of drying and the stresses it creates, fracture can be neither understood nor fully controlled.

In this Letter, we present a comprehensive physical picture of the fluid to solid transition induced by drying, which agrees quantitatively with observations of the dynamics of solidification in colloidal suspensions constrained to dry from one end. We show that the dynamics of drying are determined by a blend capillary and viscous forces, regulated by the nanometer-scale texture of the air-water interface. Interestingly, as the radii of suspended particles are decreased, the macroscopic dynamics of drying show signatures of molecular-scale fluid effects.

We observe the drying of aqueous suspensions of monodisperse colloidal silica with radii,  $a$ , from 6 to

26 nm. Glass or sapphire capillary tubes, with dimensions  $\Delta x = (1-10)$  mm,  $\Delta y = (1-4)$  cm,  $\Delta z = (30-100)$   $\mu\text{m}$ , are filled from one end, with the inner meniscus at least 5 mm from the opposite end. The air inside the capillary rapidly saturates with water vapor; thus, practically all evaporation occurs from the filling end,  $y = 0$ , as shown in the inset to Fig. 1. Within minutes, a striking array of cracks can be seen by the eye, invading the sample from the drying edge. Additional features are visible with bright field microscopy. The volume fraction of nanoparticles changes abruptly slightly ahead of the crack front; the sharp gradient in index of refraction makes this *compaction front* visible as the dark band labeled *A* in Fig. 1. There is a sharp drop in transmitted light near the crack tips, labeled *B* in Fig. 1, due to reflections off additional interfaces as material separates from the walls.

We measure the dynamics of the crack tips to help elucidate their origin. We use a suspension of  $a = 11$  nm silica at an initial volume fraction  $\phi_D = 30\%$ , heat the sample to  $50^\circ\text{C}$ , and image the crack motion at video rates for about 2000 s. Individual crack tips display

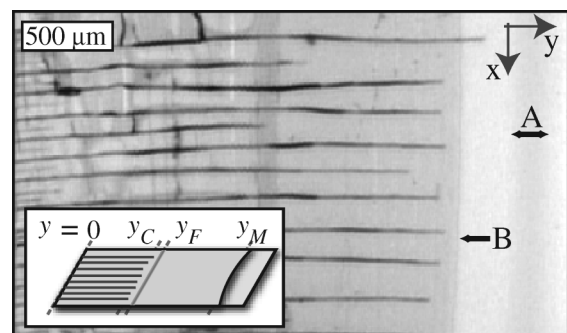


FIG. 1. Bright-field image of a drying suspension of silica nanoparticles. Inset: a schematic of the experimental geometry. Water evaporates from the drying edge,  $y = 0$ . The crack tips extend to  $y_C$ , just behind the compaction front, at  $y_F$ . The inner meniscus lies at  $y_M$ .

intriguing intermittent motion that leads to the staircase-shaped trajectories shown in Fig. 2(a). By contrast, the position of the average crack tip evolves smoothly and is well described by  $y_C = \sqrt{2D_C t}$ , with  $D_C = 8.1 \times 10^{-3} \text{ mm}^2/\text{s}$ , as shown in Fig. 2(b). This suggests an underlying diffusive process, consistent with models that have been proposed to explain the crack spacing [4,5]. However, this interpretation must be questioned due to recent elastostatic calculations, motivated by observations of fracture saturation in geological and engineering problems, which show that crack spacing can be surprisingly independent of system details [9,10].

A critical test of the role of diffusion is the distribution of water: If fluid diffuses to the drying surface, there should be a smooth gradient in the water concentration from the compaction front to the drying edge. To investigate this, we directly image the water with laser-scanning coherent anti-Stokes Raman scattering (CARS) microscopy [11,12]. Tuning the CARS microscope to  $3500 \text{ cm}^{-1}$ , in the OH stretching region of water, we find that the compaction front is the transition between a solid region with a high particle volume fraction and a fluid region with a low particle volume fraction. With the exception of the cracks, which are dry, both the solid and fluid regions are wet. In addition, the water concentration is uniform within each region. Thus, the concentration gradient necessary for diffusion is not present. This casts doubt on drying models incorporating diffusive fluid transport.

To test further the role of diffusion, we compare the growth of the compact region in drying suspensions of various particle radii at ambient temperature and humidity. Surprisingly, the compaction front follows qualitatively different trajectories as the radius of suspended particles changes. Assuming  $y_F \sim t^\nu$ , we find that  $\nu$  varies from 0.5 to 0.9 as  $a$  increases from 6 to 26 nm, as shown in Fig. 3(a). The departure from  $\nu = 0.5$  con-

firms that diffusion cannot be the underlying mechanism of fluid transport.

These data demand an alternate explanation. We propose that capillary forces drive the flow of fluid to the drying surface. As water evaporates, strong particle wetting prevents the invasion of air into the sample. Rather, evaporation pockmarks the interface with nanomenisci. These create capillary tension that pulls water through the solid to replace that lost by evaporation, keeping the particles wet and the air-water interface fixed at the first layer of spheres. The capillary pressure,  $P_C(r_M) = -2\gamma/r_M$ , can be enormous. In close-packed spheres, the radius of curvature of the nanomenisci,  $r_M$ , can be as small as the minimum pore radius,  $r_P^{\text{min}} \approx 0.15a$ . Using the air-water surface tension  $\gamma \approx 0.07 \text{ N/m}$  and  $a = 11 \text{ nm}$ , the pressures in the fluid can be as low as  $-800 \text{ atm}$ . The rate of fluid flow through the compact region,  $J_F$ , must balance the evaporation rate,  $J_E$ , to keep the air-water interface fixed at the drying edge. The fluxes

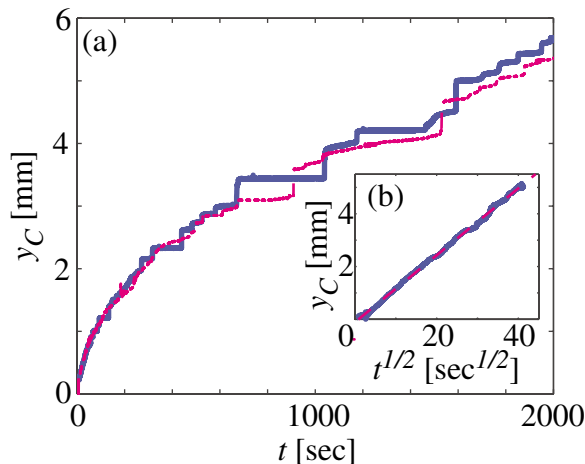


FIG. 2 (color online). (a) Trajectories of the tips of two cracks in the same sample. (b) The average position of all the crack tips in a single sample plotted against the square root of time.

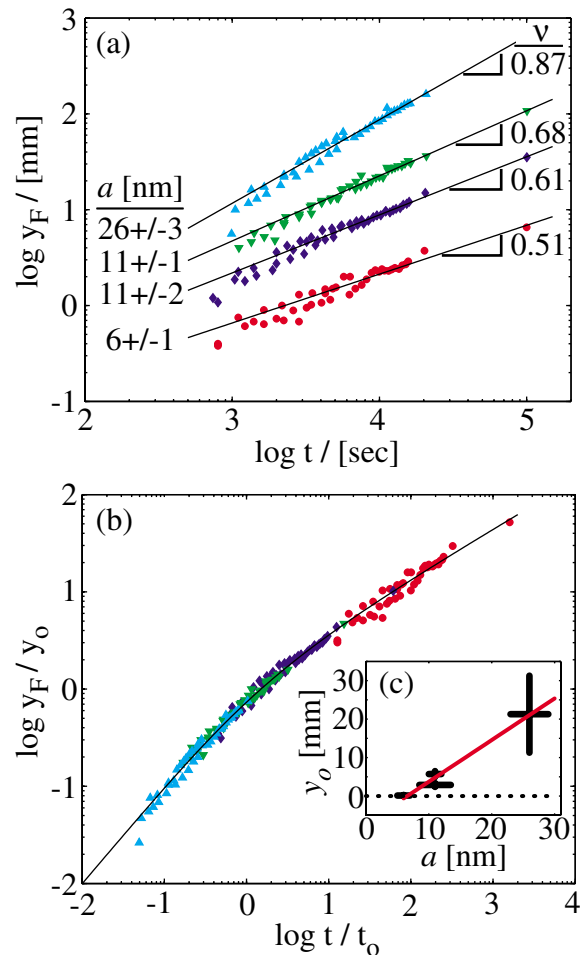


FIG. 3 (color online). (a) Compaction front trajectories in suspensions of spheres with radii from 6 to 26 nm, offset for clarity. (b) When scaled by fitted values of  $y_0$  and  $t_0$ , the trajectories collapse onto the predictions of Eq. (2), solid line. (c) The dependence of the crossover length,  $y_0$ , with sphere radius,  $a$ .

$J_E$  and  $J_F$  are measured in volume of fluid per unit area per time and have units of velocity. This allows us to determine the fluid flow in the sample and the growth of the compact region.

Fluid flow deposits additional particles in the compact region and is determined by a balance of capillary pressure and viscous resistance to flow through the compact region [13–15]. We use Darcy’s law to describe the fluid flow,  $J_F = -\frac{k}{\eta}\nabla P$ , where  $\eta$  is the fluid viscosity and the permeability,  $k$ , captures the geometry of the porous compact region. For randomly packed monodisperse spheres, the permeability can be estimated using the Carmen-Kozeny equation,  $k = \frac{1}{45}\frac{(1-\phi_C)^3}{\phi_C^2}a^2$ , where  $\phi_C$  is the particle volume fraction [8]. Assuming that the compact region is homogeneous, the pressure gradient is uniform and equal to the ratio of capillary pressure to the length of the compact region  $P_C(r_M)/y_F$ .

A measurement of the volume fraction in the compact region,  $\phi_C$ , is required to estimate  $k$ . This is determined by comparing the relative motions of the compaction front, at  $y_F$ , and the inner meniscus, at  $y_M$ . Mass conservation requires that  $\Delta y_F = \frac{\phi_D}{\phi_C - \phi_D}\Delta y_M$ . Measuring  $\Delta y_F$  and  $\Delta y_M$  for a suspension of  $a = 11$  nm spheres with  $\phi_D = 16\%$ , we find that  $\phi_C = (58 \pm 8)\%$ , implying that the compact region is close packed and the volume occupied by cracks is negligible.

The rate of fluid evaporation is set by the diffusion-limited transport of water vapor from the drying edge and can be suppressed by the nanometer-scale texture of the air-water interface. The evaporative flux from a smooth air-water interface is proportional to the gradient of the vapor concentration,  $J_0 \sim -D_V\nabla P_V$ , where the diffusion coefficient of water vapor,  $D_V = 2 \times 10^{-5}$  m<sup>2</sup>/s and  $P_V$  is the pressure of the water vapor. For low ambient humidity, the pressure gradient can be estimated as the ratio of the saturation vapor pressure of water,  $P_S = 3 \times 10^3$  Pa, to the shortest dimension of the opening of the container,  $L$ . Therefore, the smooth interface evaporation rate is  $J_0 \approx \frac{1}{n_L k_B T} \frac{D_V P_S}{L}$ , where  $n_L$  is the number density of water molecules in the liquid state. For  $L = \Delta z = 0.1$  mm,  $J_0 = 5$   $\mu$ m/s. However, nanomenisci curvature suppresses evaporation; Kelvin’s law gives  $J_E(r_M) = J_0 \exp[-r_{M0}/r_M]$  [8]. This effect becomes important when the radius of curvature becomes comparable to molecular scales,  $r_{M0} = \frac{\gamma}{n_L k_B T}$ . For water at room temperature,  $r_{M0} \approx 0.5$  nm. Evaporation from the drying edge dominates over evaporation inside the cracks, where the humidity is high.

The overall fluid transport is determined by the combination of two mechanisms: evaporation at the drying edge and fluid flow through the compact region. This leads to two qualitatively different regimes of drying. Initially, the compact region presents negligible resistance to flow. Thus, the evaporation rate is constant and limited by diffusion of vapor from the drying surface.

However, as the compact region grows, so does its resistance. Eventually, this resistance limits the evaporation rate. The characteristic length of the compact region,

$$y_0 = \frac{k}{\eta J_0} \frac{2\gamma}{r_P^{\min}}, \quad (1)$$

determines the crossover from the *evaporation-limited* to the *flow-limited* regime. The evaporation rate is constant when  $y_F \ll y_0$  and falls when  $y_F \gg y_0$ . Physically, the evaporation rate falls when the nanomenisci attain their minimum radii of curvature, after which the growing viscous resistance of the compact region dominates the fluid transport. In practice, the location of the crossover can be tuned by varying the particle size, solvent viscosity, ambient humidity, or temperature. A crossover from constant to falling evaporation rates is also seen in drying gels but occurs when the air-water interface moves from the edge of the sample and into the bulk [8].

This picture captures the full range of dynamics of the compaction front. Since the rate at which water leaves the system,  $J$ , is limited by the slower of the flow and evaporation rates, we write  $J^{-1} = J_E^{-1} + J_F^{-1}$ . Neglecting Kelvin’s law, this gives  $J(y_F) = J_0 y_0 / (y_0 + y_F)$ . Noting that  $J = dy_M/dt$  and applying our expressions for mass conservation and  $J(y_F)$ , we solve for  $y_F(t)$  to yield

$$\frac{y_F(t)}{y_0} = \sqrt{1 + 2t/t_0} - 1, \quad (2)$$

where  $t_0 = \frac{\phi_C - \phi_D}{\phi_D} \frac{y_0}{J_0}$ . During the evaporation limited regime,  $t \ll t_0$ , and  $y_F \sim t$ . During the flow-limited regime,  $t \gg t_0$ , and  $y_F \sim \sqrt{t}$ . There is a broad crossover between the two regimes, which accounts for the range of exponents in Fig. 3(a). Moreover, assuming that crack propagation is limited by the growth of the compaction front, the time dependence of the flow-limited regime accounts for the apparent diffusive trajectory of the crack front shown in Fig. 2(b).

We explore the full extent of the crossover between the evaporation-limited and the flow-limited regime by measuring the trajectory of the compaction front for samples with  $a = 11$  nm, and varying only in  $\phi_D$ . As expected, the compaction front moves at a constant velocity at the lowest  $\phi_D$  and early times, as shown by the dotted line of slope  $\nu = 1$  in Fig. 4(a). By contrast, the trajectory follows  $y_F \sim \sqrt{t}$  for the highest  $\phi_D$  and latest times, indicated by the dotted line of slope  $\nu = 0.5$  in Fig. 4(a). Scaling each trajectory by fitted values of  $y_0$  and  $t_0$  leads to an excellent collapse of the data onto Eq. (2), as shown in Fig. 4(b). The crossover length is roughly constant for all dilutions,  $y_0 = (1.3 \pm 0.2)$  mm, as shown in Fig. 4(c). By comparison, using  $\phi_C = 64\%$  and macroscopic values of surface tension and viscosity, our model predicts a later crossover,  $y_0 \approx 5$  mm.

To determine the origin of this discrepancy, we analyze the compaction front trajectories of suspensions with different particle radii, shown in Fig. 3(a), to measure

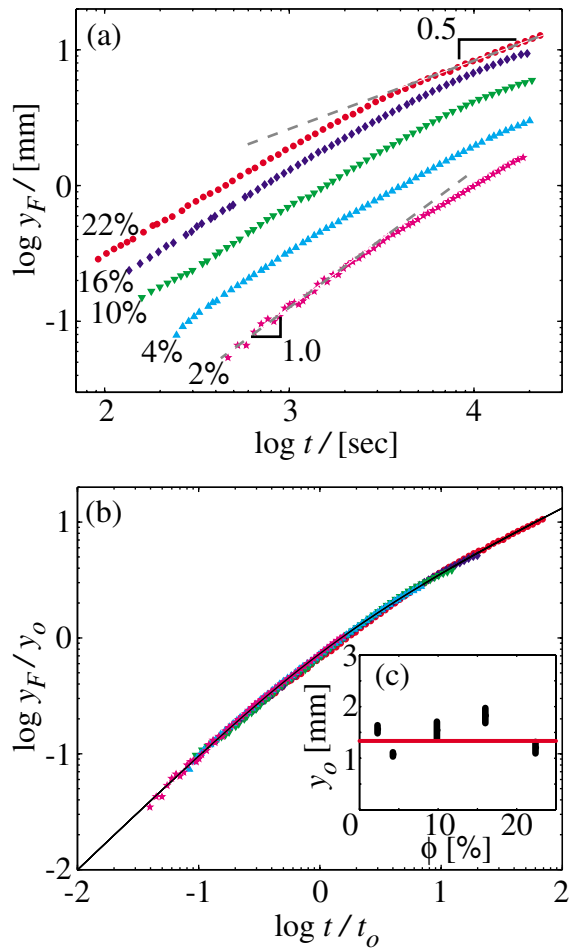


FIG. 4 (color online). (a) Compaction front trajectories in suspensions varying only in initial volume fraction. (b) When scaled by fitted values of  $y_0$  and  $t_0$ , the trajectories collapse onto the predictions of Eq. (2), solid line. (c) The dependence of the crossover length,  $y_0$ , with the initial volume fraction,  $\phi_D$ .

the variation of  $y_0$  with  $a$ . Once again, scaling the trajectories by fitted values of  $y_0$  and  $t_0$  collapses the data onto Eq. (2), as shown in Fig. 3(b). Our model predicts that the crossover length should scale linearly with particle size,  $y_0 = \alpha a$ . However, we observe that  $y_0 = \alpha(a - a_0)$ , as shown in Fig. 3(c), with  $a_0 = (5.9 \pm 2.8)$  nm and  $\alpha = (1.0 \pm 0.3) \times 10^6$ . Physically, the cutoff,  $a_0$ , represents a minimum particle radius below which flow and hence evaporation stop. At this cutoff,  $r_p^{\min} = (9.2 \pm 4.4)$  or  $(6.5 \pm 3.1)$  Å molecular radii. Geometry places a lower bound on the cutoff: When the particles are too small, water molecules can no longer fit through their interstices. Liquid structure and fluid-substrate interactions can also increase the cutoff pore size. If we assume that the macroscopic viscosity holds above the cutoff, then our drying model predicts  $\alpha \approx 5 \times 10^5$ , which is close to the observed value. This behavior is qualitatively consistent with recent molecular dynamics simulations [16] and surface forces apparatus measurements [17,18], and may be related to non-Darcy

flow observed in dense clays [19]. The simple physical picture presented here, which combines the granularity of fluids with a naive extension of macroscopic fluid mechanics, captures the essential physics.

We have found that the macroscopic dynamics of drying nanoparticle suspensions, observable with a micrometer and a stopwatch, depend sensitively on molecular-scale physics. This is a clear demonstration of how molecular-scale fluid effects can alter the macroscopic dynamics of real systems of technological importance. Furthermore, our approach provides a simple and robust platform for investigating molecular-scale fluid transport, which could have implications for nanofluidic devices and the transport of molecules across biological membranes.

We thank M. Brenner, S. Mazur, J. Rice, H. Stone, and G. Scherer for helpful comments and the NSF for funding through the Harvard MRSEC (DMR-03-13805).

\*Current address: Department of Physics, University of Chicago, Chicago, IL.

†Current address: Department of Physics, University of Massachusetts, Amherst, MA.

- [1] M. Egen and R. Zentel, *Chem. Mater.* **14**, 2176 (2002).
- [2] K. Shorlin, J. deBruyn, M. Graham, and S. Morris, *Phys. Rev. E* **61**, 6950 (2000).
- [3] Z. Neda, K.-t. Leung, L. Jozsa, and M. Ravasz, *Phys. Rev. Lett.* **88**, 095502 (2002).
- [4] C. Allain and L. Limat, *Phys. Rev. Lett.* **74**, 2981 (1995).
- [5] T. Komatsu and S. Sasa, *Jpn. J. Appl. Phys., Part 1* **36**, 391 (1997).
- [6] D. Hull and B. D. Caddock, *J. Mater. Sci.* **34**, 5707 (1999).
- [7] L. Pauchard, M. Adda-Bedia, C. Allain, and Y. Couder, *Phys. Rev. E* **67**, 027103 (2003).
- [8] C. Brinker and G.W. Scherer, *Sol-Gel Science: The Physics and Chemistry of Sol-Gel Processing* (Academic Press, New York, 1990).
- [9] T. Bai, D. Pollard, and H. Gao, *Nature (London)* **403**, 753 (2000).
- [10] M. Adda-Bedia and M. Ben Amar, *Phys. Rev. Lett.* **86**, 5703 (2001).
- [11] A. Zumbusch, G. Holtom, and X. Xie, *Phys. Rev. Lett.* **82**, 4142 (1999).
- [12] J. Cheng, Y. Jia, G. Zheng, and X. Xie, *Biophys. J.* **83**, 502 (2002).
- [13] R. Deegan, O. Bakajin, T. Dupont, G. Huber, S. Nagel, and T. Witten, *Nature (London)* **389**, 827 (1997).
- [14] A. F. Routh and W. B. Russel, *Ind. Eng. Chem. Res.* **40**, 4302 (2001).
- [15] D. Kang and N. Clark, *J. Korean Phys. Soc.* **41**, 817 (2002).
- [16] R. Allen, S. Melchionna, and J.-P. Hansen, *Phys. Rev. Lett.* **89**, 175502 (2002).
- [17] U. Raviv, P. Laurat, and J. Klein, *Nature (London)* **413**, 51 (2001).
- [18] Y. Zhu and S. Granick, *Phys. Rev. Lett.* **87**, 096104 (2001).
- [19] J. Byerlee, *Geophys. Res. Lett.* **17**, 2109 (1990).